2024

Bending Mechanics of Bio-mimetic Stiff Scale-Covered Plate

Pranta Rahman Sarkar
University of Central Florida

BENDING MECHANICS OF BIO-MIMETIC STIFF SCALE-COVERED PLATE

by

PRANTA RAHMAN SARKAR
B.S. Bangladesh University of Engineering and Technology, 2018

A thesis submitted in partial fulfilment of the requirements
for the degree of Master of Science
in the Department of Mechanical and Aerospace Engineering
in the College of Engineering and Computer Science
at the University of Central Florida

Summer Term
2024

Major Professor: Ranajay Ghosh

ABSTRACT

Biomimetic scale-covered systems offer immense potential and applications, particularly in soft robotics, protective armors, wearable materials, and multifunctional aerospace structures. A typical system consists of stiff rectangular plate like scales embedded in a softer media and arranged periodically. Experimentally, these systems indicate pronounced nonlinear strain stiffening behavior even when the underlying substrate strains are small. However, capturing these behaviors using commercial finite element (FE) codes has proved difficult due to multiple sliding contacts between the scales after engagement. Therefore, accurate and reliable analytical models of architecture-property-relationships are needed for analysis and design. This thesis investigates the contact kinematics and mechanics of biomimetic scale-covered plates subjected to bi-directional bending. Both synclastic and anti-clastic deformations of the plate are considered. The mechanical moment-curvature relationships are derived using the work-energy balance principle. The results show that when a plate is bent to a certain curvature, a quasi-rigid locked emerges for both synclastic and anticlastic curvature. Interestingly, while for anticlastic bending, the curvature at locking is nearly the same curvature as a beam with equivalent geometry and configuration, for synclastic bending, locking occurs significantly earlier due to cross-curvature effects. The moment-curvature relationships indicate strongly anisotropic behavior of the plate. The anisotropy itself was not constant, being strongly influenced by the state of deformation. The effect of scale arrangement parameters (lattice geometry) directly influenced the nonlinear behavior including the locked state. The analytical models developed are compared with equivalent FE analysis for validation for select cases and excellent agreements have been found. The outcome of this work would enhance the understanding of the nonlinear and anisotropic behavior of scale-covered plate systems, paving the way for systematic design and integration tailored for specific applications.

To my dearest niece, whom I love most in this world.

ACKNOWLEDGMENTS

I would like to express my deepest gratitude to my adviser, Dr. Ranajay Ghosh, for his constant guidance and support throughout my graduate studies and research. His invaluable insights and mentorship have been instrumental in shaping this work, and I have gained a wealth of knowledge under his supervision.

I am also deeply grateful to my colleagues for their continuous support during my graduate journey. I would like to extend special thanks to Dr. Hossein Ebrahimi, who provided essential instruction in using ABAQUS software for finite element simulation. Additionally, I appreciate the support from Md Shahjahan Hossain and Omid Bateniparv, whose assistance was invaluable during the completion of this thesis.

Lastly, I am profoundly thankful to my family for their unwavering love and support, which have been the cornerstone of my perseverance and success.

TABLE OF CONTENTS

LIST OF FIGURES

CHAPTER 1: INTRODUCTION

Scales found in fish, reptiles, and some mammals serve various essential functions in nature. These functions include aiding in swimming and locomotion, providing camouflage, regulating thermal conditions, and offering robust protection against predators [1, 2, 3, 4, 5, 6, 7, 8, 9, 10, 11, 12, 13, 14]. The mechanical benefits of these scales are not merely due to their role as a protective layer; they largely arise from the complex interactions and sliding motions between the scales and the substrate beneath them. Factors such as arrangement, engagement, overlap, orientation, and distribution are critical in determining the mechanical performance of these scales [15, 16, 17]. Initial theoretical models demonstrated that the periodic or locally periodic arrangement of scales facilitates coordinated sliding, which enhances the system's nonlinearity, leading to substantial strain stiffening and eventually a quasi-rigid locked state [18, 19, 20]. Further studies expanded this understanding by showing that these contact nonlinearities result in various complex mechanical behaviors. These behaviors include nonlinear elasticity during twisting [20], increased resistance to puncture [21, 22, 23, 24], greater fracture resistance [25, 26], dual frictional properties [27], and emergent damping viscosity [28]. These unique mechanical properties offer several advantages over traditional composites, such as creating substrates with adjustable mechanical properties, including variable stiffness and flexibility [29], and designing structures highly resistant to buckling [30], making them suitable for a wide range of engineering applications.

Extensive studies in early literature examined the role of nonlinear contact kinematics in developing nonlinear elasticity in 1D structures, particularly in beams covered with scales. These studies often assumed that scales were either rigid or slightly flexible. Key discoveries indicated that bending [19] and twisting [20] of a 1D scale-covered substrate induce reversible nonlinear strain stiffening and jamming behavior even at small strains. Additionally, the combination of bending and twisting [31] has been shown to produce unique effects distinct from individual loading sce-

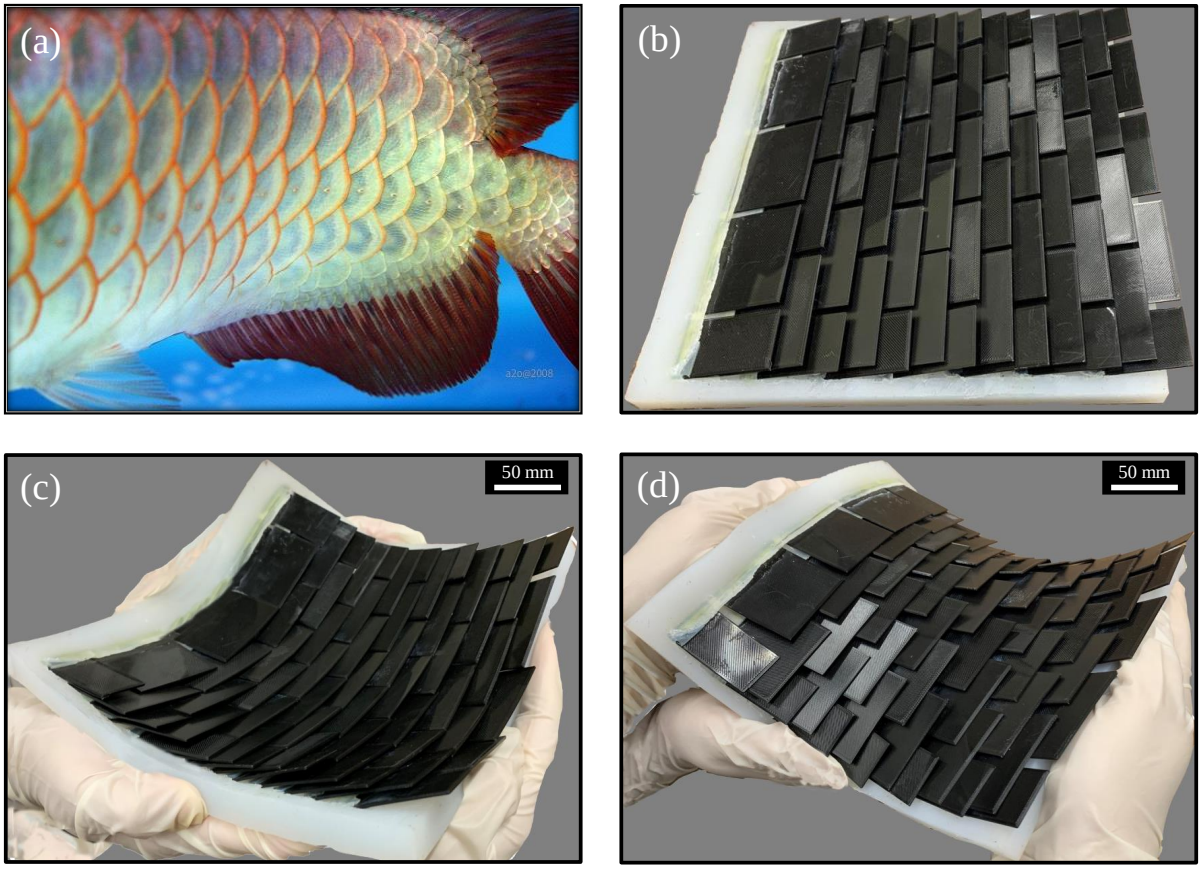

Figure 1.1: (a) A natural fish showing the tightly interlocked arrangement of its scales that provides flexibility and protection. (b) An artificially fabricated 3D fish scale structure designed to mimic natural fish scales, with the scales arranged in a staggered manner. (c) Synclastic bending deformation of the scale-covered plate, showing bending with a positive curvature in both principal directions. (d) Anticlastic bending deformation of the scale-covered plate, showing bending with opposite curvatures along two principal directions.

narios, primarily due to the complex, often non-commutative engagement patterns between the scales. Although friction can enhance these effects, it does not fundamentally change the underlying contact kinematics [27, 32]. The overall engagement patterns remain relatively consistent even when periodicity conditions are relaxed [33, 34] or other non-ideal effects are introduced [35], with models that incorporate these factors showing better alignment with numerical simulations. Analytical models remain essential due to the limitations of commercial FE-based computational

codes. To overcome these limitations, recent research has utilized the discrete element method (DEM) for computational analysis of scale-covered 1D substrates [36, 30]. This method has proven effective in addressing computational challenges and has been extended to study granular crystals [37], demonstrating tunable mechanical properties. The interface-enhanced discrete element model (I-DEM) [38] further advances DEM by incorporating interfacial interlocking and failure mechanisms, enabling accurate modeling of bio-inspired flexible protective structures. Despite significant progress in understanding the mechanics of beam-like substrates, 2D plate and shell-type systems present unique challenges due to their complex cross-curvature couplings, emergent anisotropy, and intricate scale sliding kinematics.

However, the study of plate-like systems (Figure 1(b)) is less advanced, with significant gaps in analytical modeling. Recently, there has been an increased focus on these systems, including the development of novel computational frameworks that address existing limitations in simulation capabilities and provide new insights into anisotropic behavior [39]. Computational studies utilizing conventional Lagrangian FE [29] have also highlighted unique anisotropic engagement patterns based on the scale arrangement and applied loads, aligning well with experimental observations reported in literature [40]. Advances in fabrication techniques, such as 3D printing for optimized geometries [21, 41] and vibration-driven assembly for creating topologically interlocked panels from polyhedral building blocks [42], have opened new possibilities. Additionally, hybrid armor designs incorporating polymeric and fluid-filled layers have demonstrated enhanced impact resistance [43]. These fabrication innovations pave the way for novel applications, including instability suppression [44] and combining flexibility with strength [45].

Research on 2D biomimetic structures has revealed behaviors distinct from 1D counterparts, particularly regarding biaxial asymmetries and cross-curvature couplings, which become more pronounced with plate-like bending. This thesis aims to address these challenges by developing an analytical model that examines the coupling effects of bending loads along two in-plane axes in

a biomimetic scale-covered elastic plate. By extending the mechanics from 1D to 2D structures, this study seeks to enhance the understanding of the nonlinear and anisotropic behavior of scale-covered systems. However, there is a significant gap due to the absence of accurate and reliable analytical models for 2D systems. This thesis introduces an analytical model for the 2D scale-covered plate, exploring its impact on the nonlinear elasticity of the substrate under bending deformation. The model assumes rigid scales and the kinematics and mechanics of the plate are developed for both synclastic (Figure 1(c)) and anticlastic (Figure 1(d)) deformation modes. The kinematic formulation is extended to analyze locking behavior along both longitudinal and lateral directions of the plate. The model confirms theoretical results with finite-element comparison while providing new insights into the anisotropy and non-linearity of 2D scale-covered plates under bi-directional bending. This advancement will facilitate systematic design and analysis of scale-covered plate for specific applications in fields such as soft robotics, architected structural metamaterials, protective armor, wearable technology, and aerospace structures.

CHAPTER 2: LOCKING BEHAVIOUR OF THE PLATE

In Figure 2.1, the schematic diagram of bio-mimetic scale-covered plate subjected to both synclastic and anti-clastic bending deformation is shown. The length and width of the substrate are considered as L_B and W_B, respectively, when the thickness of the plate is considered as $2t$. The exposed length of scale is assumed to be l, with width $2b$, and lateral distance between scales is assumed to be $2a$. The scales are inclined at an initial angle of θ_0. The plate is subjected to longitudinal bending M_z, and lateral bending M_x, along the longitudinal and lateral directions, respectively. Two different load cases: synclastic and anti-clastic bending modes as shown in Figures 2.1 are considered for analysis. Recently, [46] developed the kinematic relation of this 2D plate bending for both synclastic and anti-clastic deformation. In this thesis, the locking behavior of the bi-directionally bent plate has been analyzed extending the kinematic developed in [46]. The kinematic equation of a 2D plate with synclastic and anticlastic being is as follows, respectively [46]:

$$\eta \sin\psi - \sin\theta - \cos\theta\Big(\frac{\psi}{2} + (\frac{\beta+\delta}{2})\omega - \beta\sin\omega\Big) = 0. \tag{2.1}$$

$$\eta \sin\psi - \sin\theta - \cos\theta\Big(\frac{\psi}{2} + (\frac{\beta+\delta}{2})\omega - \delta\tan\omega\Big) = 0. \tag{2.2}$$

Equation (2.1) is the kinematic equation for synclastic bending, and Equation (2.2) is the kinematic equation for anti-clastic bending. Here, $\eta = l/d$, $\beta = b/d$, and $\delta = a/d$. The bending curvatures in the x-axis are called κ, which can be defined as $\kappa = \psi/d$. Also, the bending curvatures in the z-axis are τ, which is $\tau = \omega/(a+b)$. Here, ψ, and ω are the local longitudinal and transverse bending angles, respectively. In Figures 2.2, the details of the bending curvatures at the representative volume

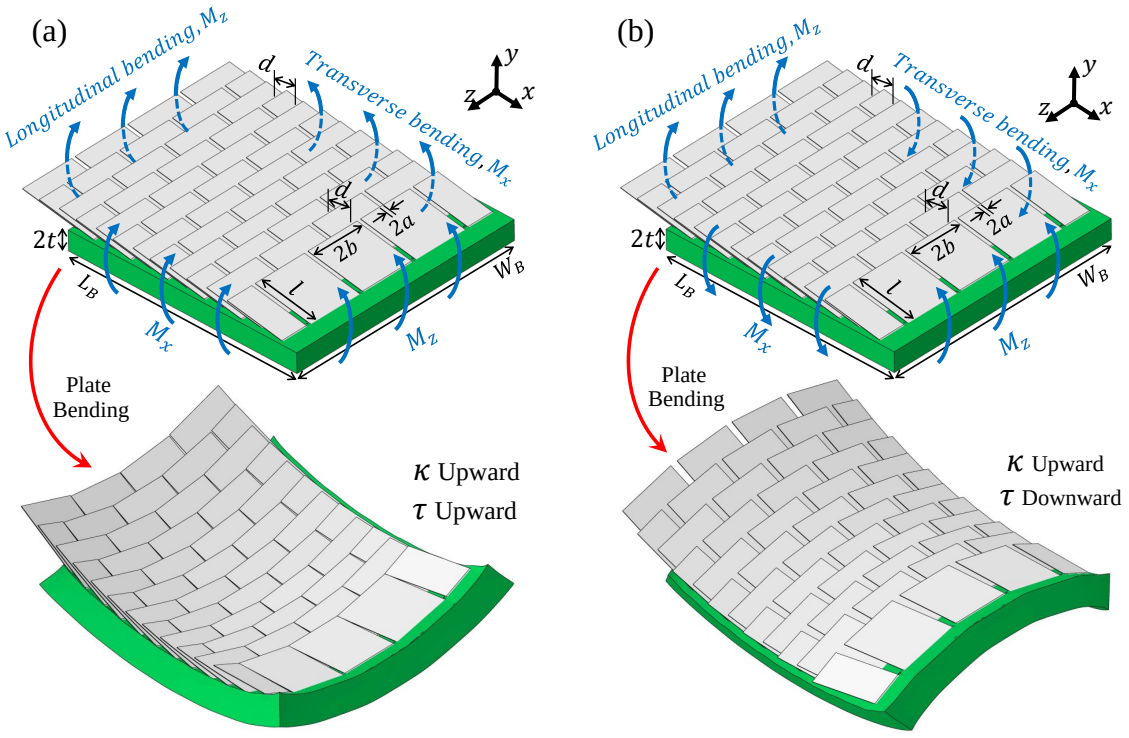

Figure 2.1: Scale-covered plate with the defined geometrical parameters under two loading cases: (a) Synclastic deformation: both curvatures are upward ($\kappa > 0$ and $\tau > 0$). (b) Anticlastic deformation: longitudinal curvature is upward ($\kappa > 0$), and transverse curvature is downward ($\tau < 0$). [46]

element (RVE) level are given for synclastic bending deformation [46]. In synclastic deformation, both curvatures are considered upward ($\kappa > 0$ and $\tau > 0$), and in anti-clastic deformation, the longitudinal curvature is kept upward ($\kappa > 0$) and the transverse curvature is downward ($\tau < 0$).

In the case of 1D beam [46], we saw when the beam is substantially bent it will reach a kinematically locked state from where no further bending is possible. A similar locking also happens for plate bending. When the plate is substantially bent it will reach a kinematically locked state. In case of 2-D plate, along with longitudinal locking, lateral locking will also take place and cross-curvature should significantly affect both the longitudinal and lateral locking of the plate. Now, to analyze the longitudinal locking response of the plate for synclastic bending deformation, we took

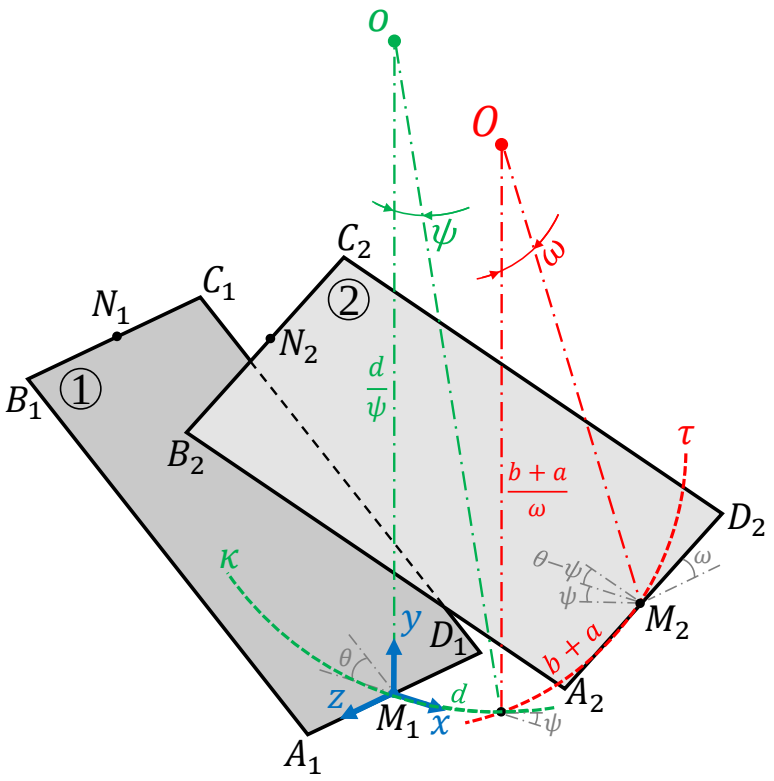

Figure 2.2: The schematic of the RVE geometrical configuration with both curvatures are upward ($\kappa > 0$ and $\tau > 0$), which means both local bending angles are positive ($\psi > 0$ and $\omega > 0$). [46]

the derivative of Equation (2.1) which is:

$$\frac{\partial \psi}{\partial \theta} = \frac{\sin\theta(\frac{\psi}{2} + (\frac{\beta+\delta}{2})\omega - \beta\sin\omega) - \cos\theta}{\frac{1}{2}\cos\theta - \eta\cos\psi}. \tag{2.3}$$

The locking curvature in the longitudinal direction of the plate is obtained by making $\frac{\partial \psi}{\partial \theta} = 0$,

$$\sin\theta(\frac{\psi}{2} + (\frac{\beta+\delta}{2})\omega - \beta\sin\omega) - \cos\theta = 0. \tag{2.4}$$

Using Equation (2.4), the rigid region of longitudinal bending is found. Similarly, for anti-clastic

bending the rigid region is found taking the derivative of Equation (2.2) with respect to θ and making $\frac{\partial \psi}{\partial \theta}$ = 0.

In case of lateral bending, locking will happen when in the lateral direction, two scales touch each other. Therefore, lateral locking is only feasible in synclastic bending, in anti-clastic bending no such lateral locking is possible. To analyze lateral locking more comprehensively, in Figure 2.2, the representative volume element of synclastic bending is shown [46]. As we see in Figure 2.1, lateral locking will happen when the top left corner of the scale shown in Figure 2.2 lies over the x-axis. At that position, the z-coordinate of that point will be zero:

$$l \sin(\theta - \psi) \sin \omega - (b + a) + b \cos \omega = 0 \tag{2.5}$$

Now, deriving θ from the above equation in terms of non-dimensional parameters:

$$\theta = \sin^{-1} \left(\frac{\delta + (1 - \cos \omega)\beta}{\eta \sin \omega} \right) + \psi \tag{2.6}$$

Substituting this expression of θ into Equation (2.1) will result the following equation:

$$\eta \sin \psi - \sin \left\{ \sin^{-1} \left(\frac{\delta + (1 - \cos \omega)\beta}{\eta \sin \omega} \right) + \psi \right\} - \cos \left\{ \sin^{-1} \left(\frac{\delta + (1 - \cos \omega)\beta}{\eta \sin \omega} \right) + \psi \right\} \left\{ \frac{\psi}{2} + \left(\frac{\beta + \delta}{2} \right) \omega - \beta \sin \omega \right\} = 0 \tag{2.7}$$

The above highly non-linear equation integrates longitudinal and lateral locking of the synclastically bent plate.

In anti-clastic bending, no lateral locking will take place in the abovementioned way, since scales

don't touch each other in lateral directions. But similar to 1D beam or synclastic longitudinal locking, here in the case of anti-clastic bending also, longitudinal locking takes place. To analyze the locking response of the plate, we took the derivative of Equation (2.2) which is:

$$\frac{\partial \psi}{\partial \theta} = \frac{\sin\theta(\frac{\psi}{2} + \frac{\beta+\delta}{2}\omega - \delta\tan\omega) - \cos\theta}{\frac{1}{2}\cos\theta - \eta\cos\psi}. \tag{2.8}$$

For locking region $\frac{\partial \psi}{\partial \theta}$ = 0,

$$\sin\theta\Big(\frac{\psi}{2} + \frac{\beta+\delta}{2}\omega - \delta\tan\omega\Big) - \cos\theta = 0. \tag{2.9}$$

Now, using the above Equation (2.9), the longitudinally locked curvature of the plate in case of anti-clastic bending is derived.

CHAPTER 3: MECHANICS OF THE PLATE

The moment-curvature relationship of the plain plate can be written in the form of stiffness matrix as:

$$\begin{Bmatrix} M_x \\ M_z \end{Bmatrix} = D \begin{bmatrix} 1 & \nu \\ \nu & 1 \end{bmatrix} \begin{Bmatrix} \tau \\ \kappa \end{Bmatrix} \tag{3.1}$$

Here, $D = \frac{Eh^3}{12(1-\nu^2)}$ is the bending rigidity of the plain plate, E is the elastic modulus, and ν is the Poisson's ratio. The scales on the substrate have an embedded part that increases the stiffness of the substrate even before engagement is achieved. This is the so-called inclusion effect, which in this case of plate changes the isotropic substrate into a composite structure. The increase in bending rigidity due to these inclusions can be modeled empirically by assuming two inclusion correction factors $C_{f,x}$, and $C_{f,z}$, similar to previous works on 1D substrates [20]. The scale-embedded plate can be modeled as a short-fiber orthotropic composite plate and thus the correction factors then lead to a new modified moment-curvature relationship:

$$\begin{Bmatrix} M_x \\ M_z \end{Bmatrix} = D \begin{bmatrix} C_{f,x} & \nu \\ \nu & C_{f,z} \end{bmatrix} \begin{Bmatrix} \tau \\ \kappa \end{Bmatrix} \tag{3.2}$$

Due to the bi-directional bending of the plate, the strain energy on the plate according to classical plate theory is:

$$\Delta U = \frac{1}{2}(M_x\tau + M_z\kappa)L_B W_B \tag{3.3}$$

With expressions of M_x and M_z from Equation (3.2):

$$\Delta U = \frac{D}{2}(C_{f,x}\kappa^2 + 2\nu\tau\kappa + C_{f,z}\tau^2)L_B W_B. \tag{3.4}$$

The work done due to bending in the longitudinal and transverse directions of a plate is represented by $W_B \int_0^\kappa M_z \, d\kappa$ and $L_B \int_0^\tau M_x \, d\tau$, respectively. This work is stored as strain energy in the plate, which is expressed as $\frac{D}{2}(C_{f,x}\kappa^2 + 2\nu\tau\kappa + C_{f,z}\tau^2)L_B W_B$. Additionally, the energy due to the rotation of scales upon engagement is given by $\frac{1}{2}N_x N_z K_\theta^*(\theta - \theta_0)^2$, where N_x and N_z are the numbers of scales along the x and z directions, respectively. After scales engagement, each scale starts to rotate due to contact with other scales, and the rotation of the scale is resisted by the elastic substrate. Likewise 1-D bending and twisting cases [19, 20], the substrate resistance is modeled as rotational springs, and the rotational spring constant K_θ^* is considered to account this effect [19, 20]. By equating the work and energy of the plate:

$$\begin{aligned} &W_B \int_0^\kappa M_z \, d\kappa + L_B \int_0^\tau M_x \, d\tau \\ &= \frac{D}{2}(C_{f,x}\kappa^2 + 2\nu\kappa\tau + C_{f,z}\tau^2)L_B W_B + \frac{1}{2}N_x N_z K_\theta^*(\theta - \theta_0)^2 H(\theta - \theta_e). \end{aligned} \tag{3.5}$$

Here, θ_e is the engagement angle of scales. To obtain the moment-curvature relationship along longitudinal direction (x-axis) of the plate, we differentiate Equation (3.5) with respect to κ:

$$W_B M_z = D(C_{f,x}\kappa + \nu\tau)L_B W_B + K_\theta^* N_x N_z(\theta - \theta_0)\frac{\partial\theta}{\partial\kappa}H(\theta - \theta_e). \tag{3.6}$$

Now, non-dimensionalizing Equation (3.6) by dividing DW_B and substituting the expression of $N_z = \frac{W_B}{2(a+b)}$:

$$\bar{M_z} = (C_{f,x}\kappa + \nu\tau)L_B + \frac{K_\theta^*}{D}\frac{N_x}{2(a+b)}(\theta - \theta_0)\frac{\partial\theta}{\partial\kappa}H(\theta - \theta_e). \tag{3.7}$$

Similarly, to obtain the moment-curvature relationship along the transverse direction (z-axis), we differentiate Equation (3.5) with respect to τ, and, then non-dimensionalize it by diving DL_B and substituting $N_x = \frac{L_B}{d}$:

$$\bar{M_x} = (C_{f,z}\tau + \nu\kappa)W_B + \frac{K_\theta^*}{D}\frac{N_z}{d}(\theta - \theta_0)\frac{\partial\theta}{\partial\tau}H(\theta - \theta_e). \tag{3.8}$$

Here, Equation (3.7) and Equation (3.8) are used to solve the moment-curvature response along x and z-axis, respectively.

To determine the values of $C_{f,x}$ and $C_{f,z}$, extensive finite-element simulations are conducted with varying embedded parameters, L, t_s, and b. The plate is considered to be with only rigid inclusions, which means, the exposed length of the scales is assumed to be 0 (so, l = 0, and therefore η = 0). In the absence of any embedded scale in the plate $C_{f,x}$ and $C_{f,z}$ are equal to 1. But for a plate with embedded rigid scale, both $C_{f,x}$ and $C_{f,z}$ should be ≥ 1. Therefore, for $C_{f,x}$ and $C_{f,z}$, two different equations as a function of four dimensionless parameters, $\zeta(= L/d), \beta(= b/d), \gamma(= \sqrt{t_s/d})$, and $\delta(= a/d)$ are considered as follows:

$$C_{f,x} = C_{f,x1} + C_{f,x2}\big(\zeta\beta\gamma\big)h(\theta_o), \tag{3.9}$$

$$C_{f,z} = C_{f,z1} + C_{f,z2}ln\big(\frac{\zeta\beta\gamma}{\delta}\big)h(\theta_o). \tag{3.10}$$

The constants $C_{f,x1}, C_{f,x2}, C_{f,z1}$, and $C_{f,z2}$ are determined using finite-element simulations as illus-

trated in Figure 3.1. These constants are derived by fitting simulation data to the best-fit equations, resulting in $C_{f,x1} = 0.98$, $C_{f,x2} = 3.72$, $C_{f,z1} = 3.27$, and $C_{f,z2} = 0.49$. The dimensionless angular function $h(\theta_0)$ is approximately 1, indicating that the initial scale inclination angle θ_0 does not significantly affect the inclusion correction factors. Also, between synclastic and anticlastic bending no variation of $C_{f,x}$ and $C_{f,z}$ are found. These equations are then utilized in the analytical expressions derived in Equation (3.7) and Equation (3.8) to determine the moment-curvature relationship of the scale-covered plate.

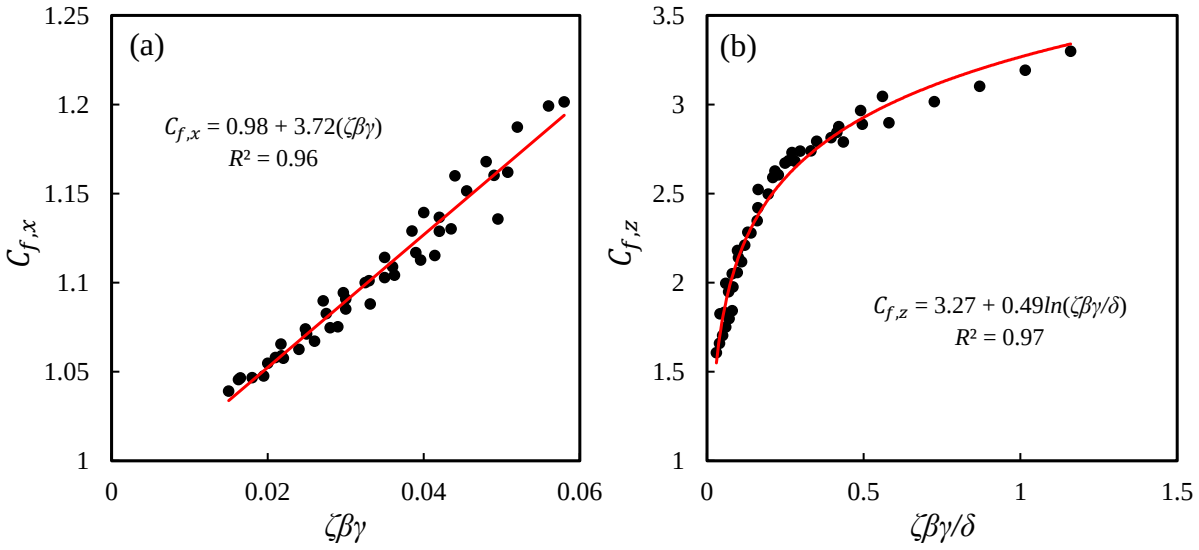

Figure 3.1: Dimensionless inclusion correction factors (a) $C_{f,x}$, (b) $C_{f,z}$ as a function of dimensionless geometrical variable group.

For rotational springs constant K_θ^*, the scale width $2b$ is considered here with previously developed scaling law K_θ [19, 33]. Thus the final expression of K_θ^* will be:

$$K_\theta^* = (2b)K_\theta = (2b)E_B t_s^2 C_b (\frac{L}{t_s})^n f(\theta_0). \tag{3.11}$$

Here, C_b = 0.66 and n = 1.75 are dimensionless constant obtained from [19]. This equation of K_θ^* differs from the 1-D case of K_θ [19] in that when we consider scale as a rigid thin plate, scale width $2b$ also needs to be considered. And dimensionless angular function $f(\theta_0) \approx 1$ indicates negligible angular dependency in case of 2-D plate.

CHAPTER 4: FINITE ELEMENT FORMULATION

An FE model is developed to compare the numerical results with those derived from the analytical model. The FE simulations are performed using the commercially available software ABAQUS/CAE (Dassault Systèmes), with dimensions and loading conditions matching those specified in the analytical model. In this model, the scales and substrate are treated as 3D deformable solids. A square plate substrate with dimensions $W_B = L_B = 64$ mm is used, which ensures periodicity and minimizes edge effects.

The specific parameters used in the model include an embedded length $L = 1$ mm, a half-scale width $b = 7$ mm, an exposed length $l = 15$ mm, a scale thickness $t_s = 0.05$ mm, and a clearance between scales $a = 0.5$ mm. These parameters yield dimensionless ratios of $\eta = 3$, $\beta = 1.4$, $\delta = 0.1$, and $L/t_s = 20$. The model consists of a staggered arrangement of 59 scales partially embedded on the substrate's top surface. The scales are oriented at an inclination angle $\theta_0 = 5^\circ$ relative to the substrate's top surface in the longitudinal direction. The scales are assumed to be rigid, while the substrate is modeled as a linear elastic material with an elastic modulus $E_B = 2.5$ MPa and a Poisson's ratio $\nu = 0.42$.

To accurately represent the rigid nature of the scales in contrast to the deformable substrate, rigid body constraints are applied to the geometry of the scales. A frictionless surface-to-surface contact interaction is defined for the surfaces of the scales. A mesh convergence study varying the approximate global size of the mesh is conducted in Figure 4.1 to determine the appropriate mesh size and density for different regions of the model, ensuring reliable numerical results. As we see in Figure 4.1, with the varying approximate global size, the strain energy distribution is well converged verifying the mesh sensitivity of FE analysis. The final mesh with approximate global size = 0.52, consists of approximately 304,000 elements, incorporating both linear tetrahedral elements (C3D4) and linear hexahedral elements (C3D8). The complex geometry of the top layer

of the substrate, which includes scale inclusions, is meshed with tetrahedral elements, while the simpler regions are meshed with hexahedral elements. Quasi-static bending loads are applied to the system in two sequential static steps. The relationship between the scales' inclination angle θ and the longitudinal bending angle ψ is investigated while maintaining a fixed transverse bending angle ω, and vice versa. In the first step, transverse rotational boundary conditions are applied to both lateral sides of the substrate in opposite directions, linearly increasing from zero to the desired value. During the second step, these transverse rotational boundary conditions are kept constant, and longitudinal rotational boundary conditions are then applied to the front and back sides of the substrate, also increasing linearly from zero.

This approach allows for a comprehensive analysis of the bending mechanics of the scale-covered plate, providing insights into the interplay between scale inclination and bending angles in both longitudinal and transverse directions. By comparing the FE model results with those from the analytical model, the study ensures the robustness and accuracy of the developed formulations.

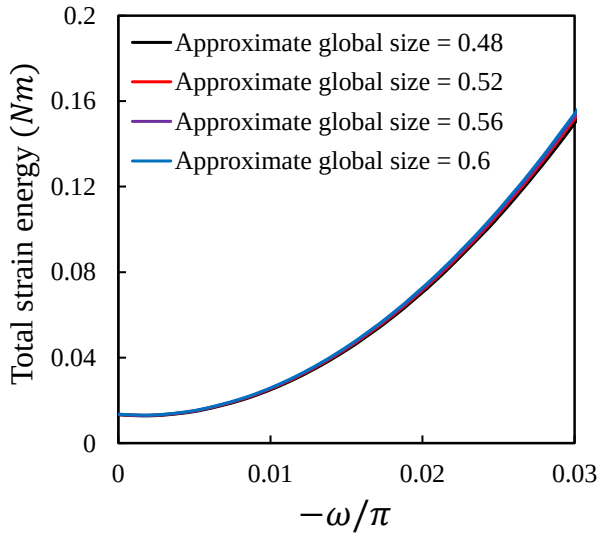

Figure 4.1: Variation of total strain energy with different FE approximate global size when ψ/π = 0.02 and $\omega/\pi < 0$. Here, $L_B = W_B = 64$ mm, θ_0 = 5°, η = 3, and β = 1.4.

CHAPTER 5: RESULTS AND DISCUSSION

5.1. Locking Kinematics of the scale-covered plate

In this section, the kinematic formulation is developed in [46] is extended to analyze the locking behavior of the scale-covered plate. As mentioned in Chapter 2, along the longitudinal direction, scales locking will also happen in the transverse directions of the plate. To analyze longitudinal locking of the plate in the presence of transverse bending, in Figure 5.1, $(\theta - \theta_0)/\pi$ distribution is plotted as a function of ψ/π with different values of η. The plate is initially assumed to be subjected to a bending curvature ω/π, then $(\theta - \theta_0)/\pi$ is plotted for $\psi/\pi > 0$. Three different values of ω/π is considered, where Figure 5.1 (a) is plotted for ω/π = 0, and Figures 5.1 (b)-(c) are plotted for ω/π = 0.08, -0.08, respectively. With Figures 5.1 (a)-(c), the longitudinal locking behavior of the plate is presented for all three deformation shapes of the plate: monoclastic, synclastic, and anticlastic, respectively. Three distinct kinematic regimes of the plate are illustrated in these plots: a linear regime before scale engagement, a nonlinear regime after scale engagement, and a locking regime where the plate behaves like a rigid body. The scale starts to engage with each other when the scale rotation angle θ is equal to θ_0, and afterward, the non-linear zone starts which continues till the rigid region. The black dashed lines in these figures represent the rigid region. To obtain the rigid region of the scale rotation, we solved $\frac{\partial \psi}{\partial \theta}$ = 0 of Equations (2.1) and (2.2). The details of this derivation are given in Chapter 2 for both synclastic and anticlastic deformation. In Figure 5.1, the corresponding ψ_{lock}/π value at the locking point is also illustrated for some particular values of η to demonstrate the exact locking curvature of the plate. As we see in Figures 5.1 (a)-(c), locking curvature is found to decrease with the increase of ω/π. The decrement is relatively noticeable for smaller η, but for higher values of η no significant variation of locking curvature with ω/π is observed even when ω/π is significantly large as 0.08. For anticlastic deformation shape with negative ω/π in Figure 5.1 (c), surprisingly no significant variation in the locking behavior is

observed compared to positive ω/π of equal magnitude.

To analyze the effect of δ on the longitudinal locking of the plate, in Figures 5.2 (a) and (b), longitudinal locking curvature ψ_{lock}/π is plotted with η and δ in the form of contour plots for two different values of ω/π. From Figure 5.2 (a), when $\omega/\pi = 0$, it is clear that the variation of δ doesn't have any effect on the longitudinal locking curvature ψ_{lock}/π of the plate. However, even with a sufficiently large ω/π = 0.08, the δ effect doesn't appear to be very significant on ψ_{lock}/π. Like synclastic bending, for anticlastic bending of the plate with negative ω/π, no significant variation of locking curvature with δ and η is observed so we omitted it to avoid overcrowding figures. Thus, from the analyses of Figure 5.1 and Figure 5.2, it can be concluded that lateral bending as well as lateral distance between scales don't have a noticeable effect on the longitudinal locking of the plate.

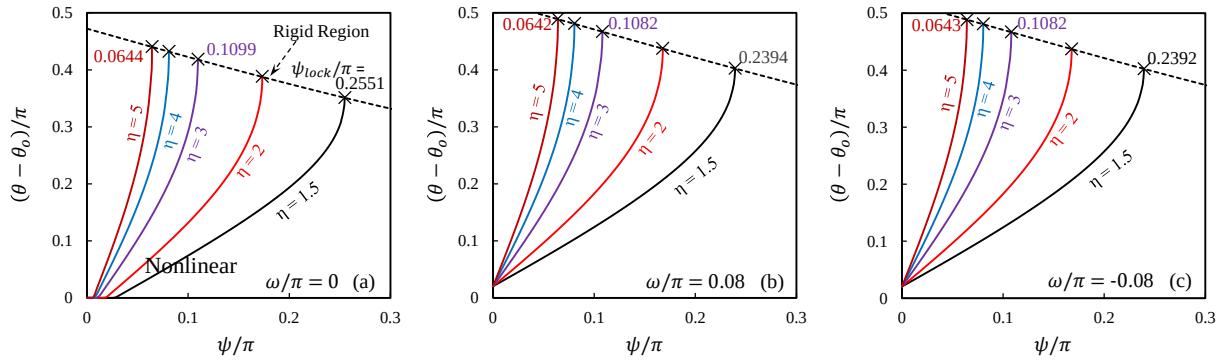

Figure 5.1: $(\theta - \theta_0)/\pi$ *vs* ψ/π variation with η when (a) ω/π = 0, (b) ω/π = 0.08, (c) ω/π = -0.08 with $\psi/\pi > 0$. Here, $\theta_0 = 5°$, and $\beta = 1.4$.

In the presence of lateral bending, the plate structure will also be laterally locked. In this thesis, the lateral locking of the plate is considered to happen at the moment scales contact with each other in the lateral direction of the plate. Therefore, lateral locking is only feasible for synclastic deformation of the plate. The detail of lateral locking for synclastic deformation is illustrated in Equation 2.7 of Chapter 2. Figure 5.3 shows the variation in scale rotation, $(\theta - \theta_0)/\pi$, with local transverse

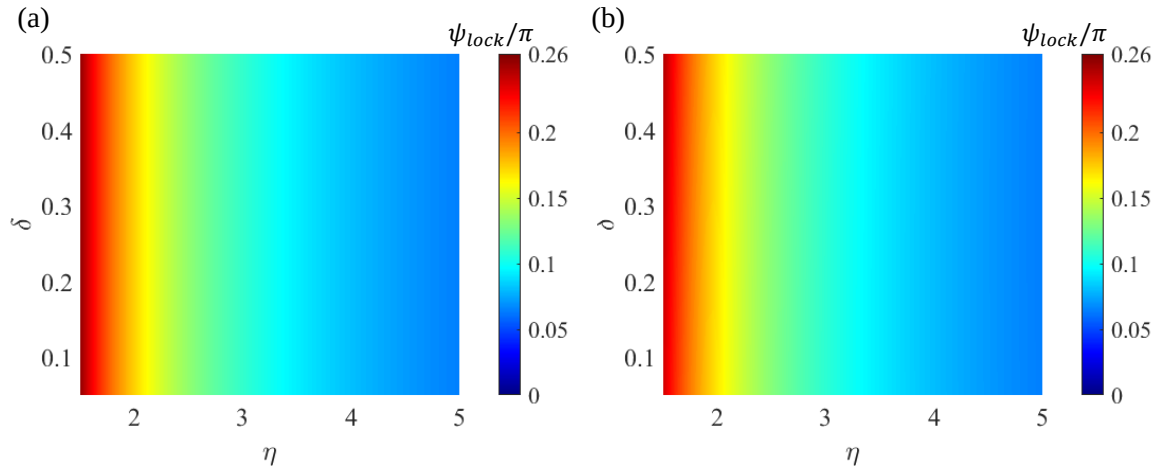

Figure 5.2: 2D image plots showing the effect of η and δ on ψ_{lock}/π, initially considering the local transverse bending angle of (a) $\omega/\pi = 0$, and (b) $\omega/\pi = 0.08$.

bending curvature, ω/π, across different values of longitudinal bending curvature, ψ/π. Initially the plate is subjected to a longitudinal curvature, ψ/π, which is then held constant while transverse curvatures ω/π (positive for synclastic and negative for anticlastic curvature) are applied. Four values of ψ/π are considered, ranging from 0 to 0.06. In both synclastic and anticlastic cases (Figures 5.3 (a) and 5.3 (b)), increasing longitudinal curvature increases scale rotation without significantly altering the slope of the $(\theta - \theta_0)/\pi$ *vs* ω/π relationship. The $(\theta - \theta_0)/\pi$ *vs* ω/π curves exhibit a linear dependence on longitudinal curvature for both deformation modes. Notably, transverse bending alone ($\psi/\pi = 0$) does not cause scale engagement. However, even minimal longitudinal bending facilitates scale engagement during transverse bending. In synclastic deformation (Figure 5.3 (a)), the transverse locking curvature decreases with increasing longitudinal curvature ψ/π, suggesting that imposed cross-curvature accelerates transverse locking. The dotted lines represent finite element (FE) results, demonstrating excellent agreement with the analytical model for both synclastic and anticlastic deformations. For a detailed illustration of the lateral locking response of the scale-covered plate, in Figures 5.4 (a)-(c), $(\theta - \theta_0)/\pi$ distribution is plotted with η for monoclastic, synclastic, and anticlastic deformation shapes, respectively. Figure 5.4 (a) is plotted for

ψ/π = 0 and $\omega/\pi > 0$, and Figures 5.4 (b) and (c) are plotted for ψ/π = 0.02 and $\omega/\pi > 0$, and ψ/π = 0.02 and $\omega < 0$, respectively. The exposed length of the scales l is varied keeping d constant to vary the values of η. As we see in Figure 5.4 (a), when ψ/π = 0, η doesn't have any effect on $(\theta - \theta_0)/\pi$ distribution of scales, but as η increases, lateral locking curvature decreases. In the presence of longitudinal bending curvature of ψ/π = 0.02, the lateral locking curvature of the plate decreases, and the decrement rate is very significant for higher values of η. Moreover, lateral locking of the plate is significantly influenced by the exposed length of the scales. With the increase of η, locking curvature drastically reduces and the presence of longitudinal bending accelerates this reduction greatly. The rigid region in Figure 5.4 (b) indicates the lateral locking curvature with η. And, as mentioned earlier, the $(\theta - \theta_0)/\pi$ distribution with η in Figure 5.4 (c) for anticlastic deformation has no lateral locking region.

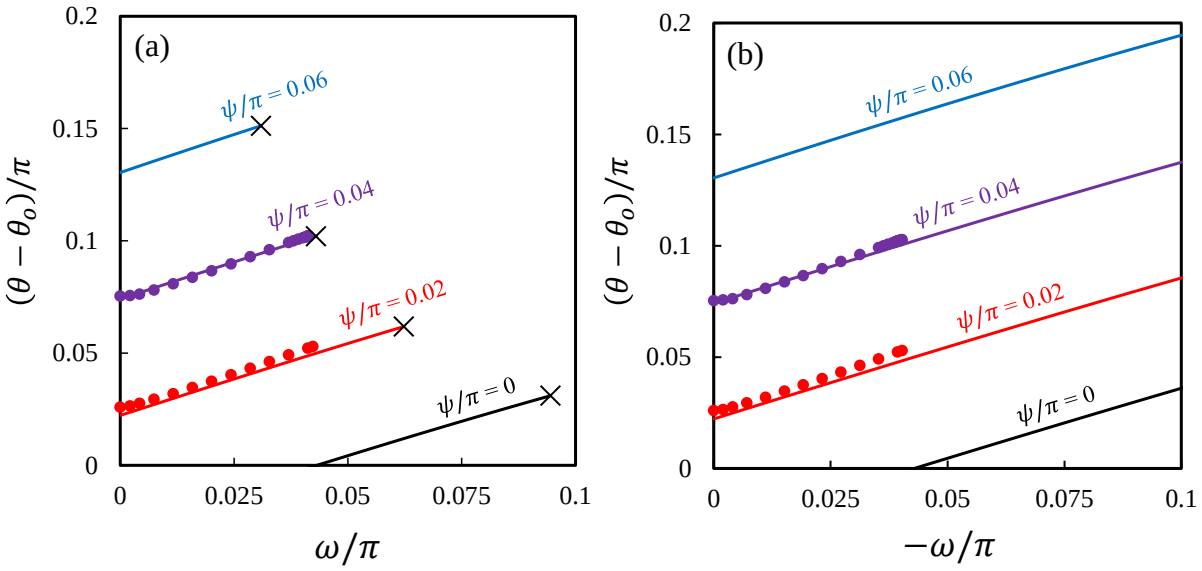

Figure 5.3: $(\theta - \theta_0)/\pi$ *vs* ω/π variation with ψ/π for (a) synclastic, and (b) anti-clastic bending deformation with the given values of $\theta_0 = 5°$, $\eta = 3$, and $\beta = 1.4$. Colored dot lines represent FE results for corresponding ψ. $(\times)$ indicates the lateral locking curvature of the plate.

In Figure 5.5, the lateral locking curvature ω_{lock}/π of the synclastically deformed plate is illustrated in the form of colored images with varying η and δ. Initially, the plate is assumed to be subjected to

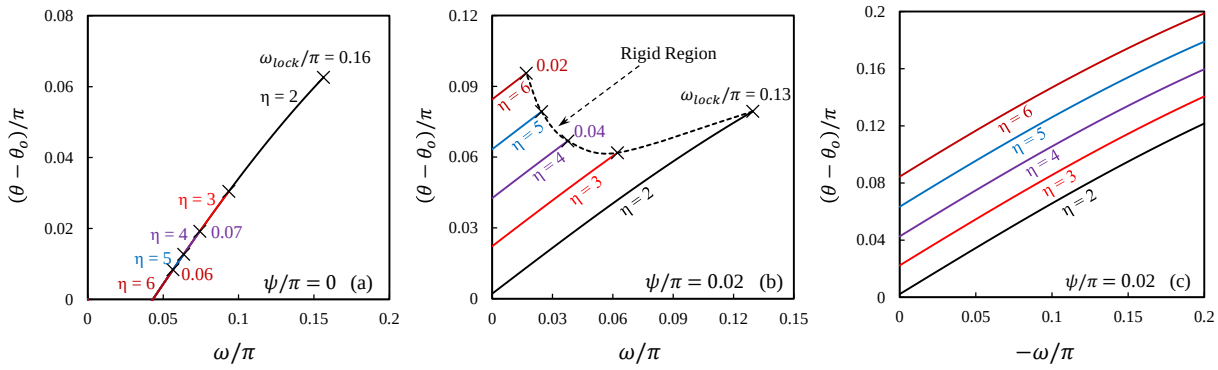

Figure 5.4: $(\theta-\theta_0)/\pi$ *vs* ω/π plot with η when (a) ψ/π = 0 and $\omega/\pi > 0$, (b) ψ/π = 0.02 and $\omega/\pi > 0$, (c) ψ/π = 0.02 and $\omega/\pi < 0$. $(\times)$ represents the lateral locking curvature of the plate. Here, $\theta_0 = 5°$, and $\beta = 1.4$.

a longitudinal curvature with three different values of ψ/π = 0, 0.03, and 0.05, and corresponding results are plotted for $\omega/\pi > 0$ in Figures 5.5 (a)-(c), respectively. As we see in Figure 5.5, for a fixed value of η, with the increase of δ, locking curvature increases, and the increment rate slows down with the increase of ψ/π. When ψ/π = 0, for small η and large δ, as we see in the top left corner of Figure 5.5 (a), the plate doesn't undergo any lateral locking, but in the presence of $\psi/\pi > 0$, that zone also starts to be laterally locked. In Figure 5.5 (c), we can see that when η = 8, the plate doesn't experience lateral locking because, with ψ/π = 0.05, the plate becomes longitudinally locked before any locking in the lateral direction. Observing all these figures, it can be concluded that, though lateral bending curvature doesn't have any significant effect on the longitudinal locking of the plate, longitudinal curvature significantly reduces the lateral locking curvature. Similarly, the lateral distance between scales doesn't have any noticeable effect on longitudinal locking but lateral locking is highly sensitive to the distance between scales in the lateral direction.

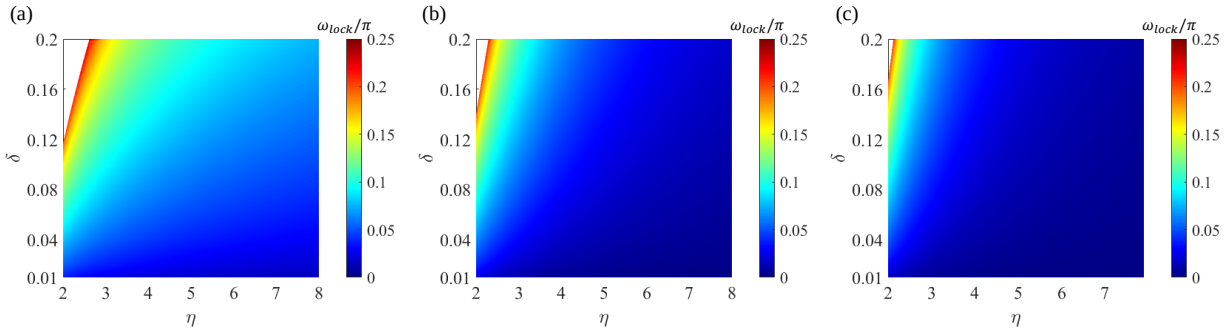

Figure 5.5: 2D image plots showing the locking curvature ω_{lock}/π with η and δ when: (a) ψ/π = 0, (b) ψ/π = 0.03, and (c) ψ/π = 0.05.

5.2. Strain energy of the Plate

To verify the work-energy balance equation of Equation 3.5, a comparison of strain energy obtained by the analytical solution using Equation 3.5 is made with FE solution in Figure 5.6. In Figures 5.6 (a) and (b), FE comparison is made with ψ/π = 0.02 for $\omega/\pi > 0$ and < 0, respectively. As the results show, for both synclastic and anti-clastic bending modes, analytical results show excellent agreement with FE results strongly verifying the work-energy balance equation. The excellent matching of strain energy distribution also strongly verifies the accuracy and reliability of the kinematics modeling of scale-covered plate. To illustrate the anisotropic behavior of the scale-covered plate on the strain energy distribution of the 2D scale-covered plate, the total strain energy of the plate is plotted in Figure 5.7 in a competitive way with the plain plate, plate with rigid scale inclusions (η = 0), and scale-covered plate with η = 3. The total strain energy is calculated using Equation 3.5 for the scale-covered plate. For plain plate and plate with rigid inclusion, the Heaviside part of Equation 3.5 is omitted. For plain plate without any scale, $C_{f,x}$ and $C_{f,z}$ values are considered as 1. As we see in Figure 5.7 (a), for the plain plate, the distribution of strain energy is symmetric diagonally, and the symmetricity is broken in the presence of scales as illustrated in Fig 5.7 (b) and (c). Also, the presence of exposed scales significantly increases the strain energy

distribution with curvature.

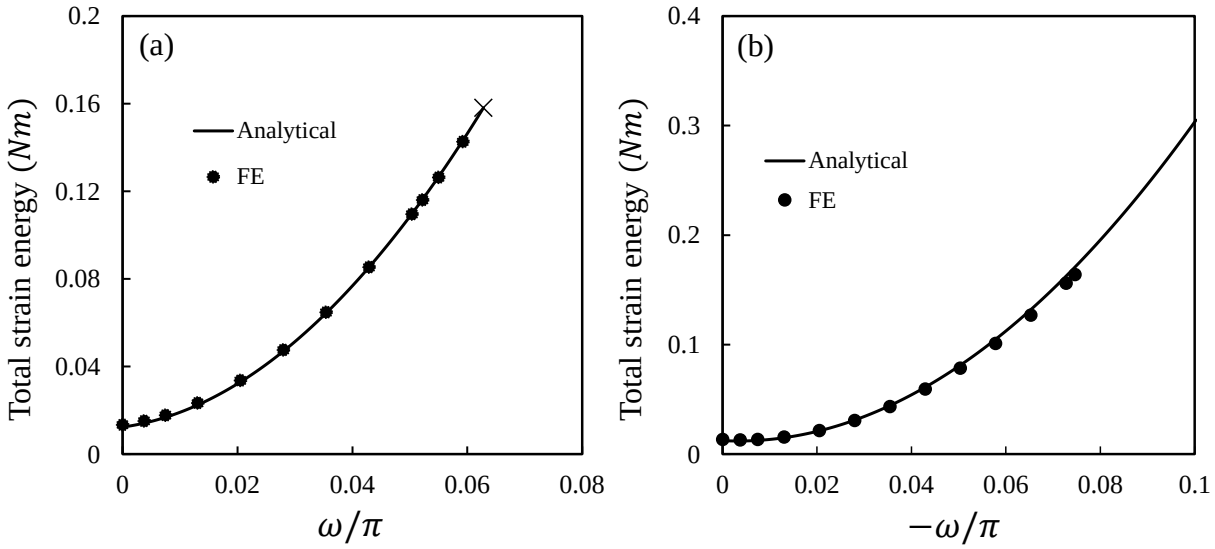

Figure 5.6: Analytical and FE results comparison for total strain energy with bending curvature of the plate when: (a) ψ/π = 0.02 and $\omega/\pi > 0$, and (b) ψ/π = 0.02 and $\omega/\pi < 0$. Here, θ_0 = 5°, η = 3, and β = 1.4. ($\times$) in Figure 5.6(a) indicates the lateral locking position of the plate.

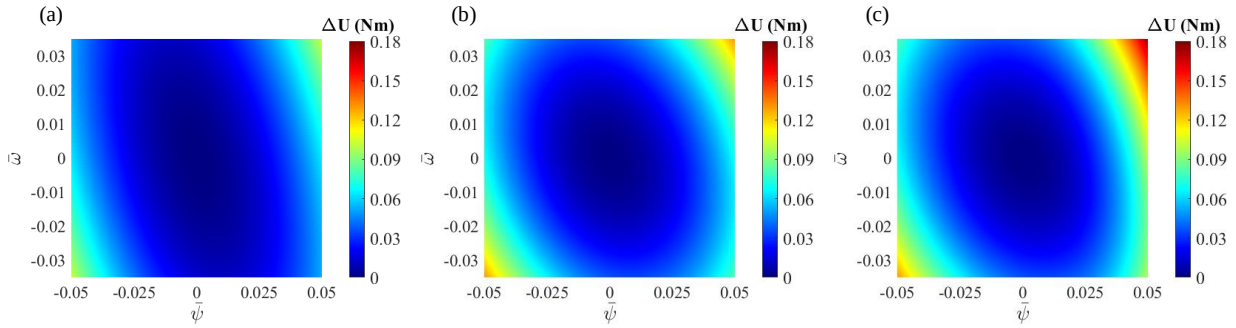

Figure 5.7: Strain energy distribution with longitudinal and transverse curvature for: (a) plain plate, (b) plate with rigid inclusion ($\eta = 0$), and (c) scale-covered plate with η = 3. Here, $L_B = W_B = 64\ (mm)$, β = 1.4, and θ_0 = 5°.

In this section, the mechanics of the scale-covered plate is presented for both synclastic and anticlastic deformation shapes with the derivation shown in Chapter 3. Figures 5.8 (a) and (b), respectively, illustrate the moment-curvature response along x-axis of the plate for synclastic and anticlastic deformation (η = 3) with four different initial values of ω/π. To analyze the effect of scale inclusion and scale engagement, a comparison with a plain plate and scale-embedded plate with η = 0 is also presented. From the moment-curvature distribution of the plain plate and plate with η = 0 (Figures 5.8 (a)), we can see that the stiffness gain only due to the presence of embedded rigid scales in the plain plate is not very significant in the longitudinal direction of the plate. But when η = 3, the engagement of rigid scales drastically increases the longitudinal moment. As ω/π increases, the engagement curvature decreases with an overall increase of moment distribution. When $\omega/\pi = 0$, initial moment in x-direction is zero, but for $\omega/\pi > 0$, there is a positive initial moment present in x-direction due to the presence of applied bending moment in z-directions and for high value of ω/π, this initial moment becomes very significant. The initial moment found in x-direction due to the bending in z-direction is because of the Poission's effect of bending. Similarly, in Figure 5.8 (b) for anticlastic deformation, when the plate is bent with negative ω/π, the initial moment due to Poisson's effect in x-direction is found to be negative. In case of anticlastic deformation, unlike synclastic bending, the effect of ω/π is very significant as we see in Figures 5.8 (a) and (b). For synclastic bending, as the slope in the moment-curvature plot with ω/π remains almost identical, ω/π doesn't show any noticeable effect on the longitudinal bending rigidity of the plate, but for anti-clastic bending ω/π drastically increases the bending rigidity of the plate in the longitudinal direction. The red dotted lines shown in Figure 5.8 (a) and (b) are obtained from finite-element simulation for ω/π = 0.03 and ω/π = -0.03, respectively. As plotted in both figures, FE result shows great agreement with the analytical results of Equation (3.7) which verifies the proper modeling of the mechanics of the plate.

In Figures 5.9 (a) and (b), the moment-curvature response along z-direction of the plate is shown for both synclastic and anticlastic deformation, respectively. Results are plotted for η = 3 initially keeping the plate fixed with four different ψ/π. In case of synclastic deformation (Figure 5.9 (a)), the moment-cuvarture distribution is plotted up to the lateral locking curvature of the plate. To analyze the effect of rigid scale inclusion, here again, results are compared with plain plate, and plate with η = 0. From the distribution of plain plate and plate with η = 0, we can see that, unlike the longitudinal moment of the plate, the presence of rigid scales is found to be very significant in the case of transverse directional moment of the plate. In absence of longitudinal bending (ψ/π = 0), η doesn't have any effect on the transverse moment distribution, and with the increase of ψ/π the nearly linear distribution of moment increases keeping the slope almost identical. Moment-curvature distribution in Figure 5.9 (a) is plotted up to lateral locking curvature of the plate for η = 3, but for η = 0, there will be no lateral locking in the plate. In the presence of longitudinal bending, the stiffness gain due to the exposed length of the scale is also clear from η = 3 and η = 0 distribution. In contrast to synclastic bending, the anticlastic deformation of the plate exhibits a negligible effect of ψ/π on the lateral moment distribution. The FE results plotted for η = 3 also show good agreement with analytical results for both loading conditions. From Figures 5.8 and 5.9, the anisotropic behavior of the plate in the presence of rigid scales is clearly reflected. As we see in Figures 5.8 (a) and 5.9 (a), M_z and M_x distribution is identical in case of plain plate since the plate is of square shape. However, the presence of scales is significantly altering the moment-curvature distribution in both directions of the square plate. Moreover, the anisotropic effect is also strongly observed in the synclastic and anticlastic deformation nature of the plate.

5.4. Effect of η and δ on the Mechanics of the Plate

Figures 5.10 (a) and (b) illustrate the effect of overlap ratio η on the moment-curvature responses of the scale-covered plate in both the x and z-directions, respectively. Five different values of η

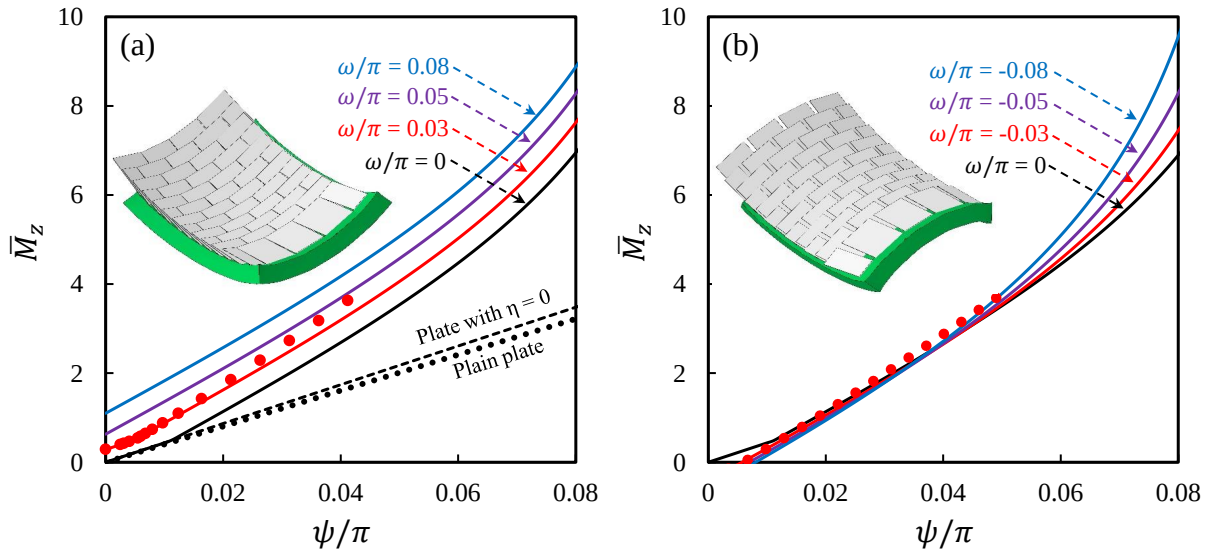

Figure 5.8: $\bar{M}_z$ *vs* ψ/π response with ω/π for (a) synclastic, and (b) anti-clastic bending deformation with $\theta_0 = 5°$, $\eta = 3$, $\beta = 1.4$, and $\delta = 0.1$. Red dot line represents FE results for ω/π = 0.03.

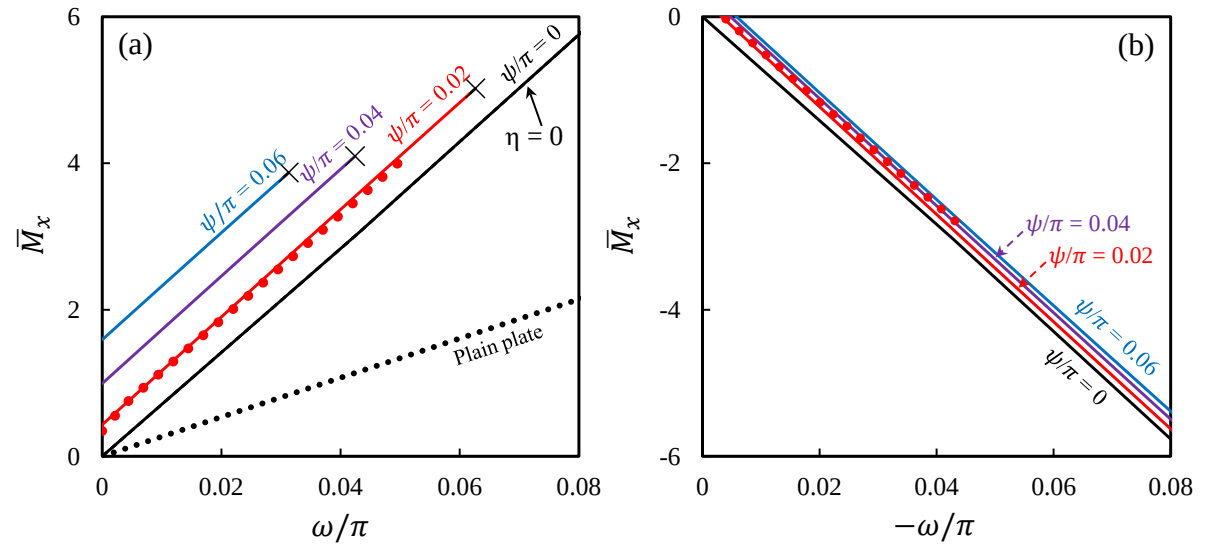

Figure 5.9: $\bar{M}_x$ *vs* ω/π and $\bar{M}_x$ vs $-\omega/\pi$ response with ψ/π for (a) synclastic, and (b) anti-clastic bending deformation with $\theta_0 = 5°$, $\eta = 3$, $\beta = 1.4$, and $\delta = 0.1$. ($\times$) indicates the lateral locking position of the plate. Red dot lines represent FE results for ψ/π = 0.02.

are considered from η = 2 - 4, wherein the exposed length of the scale l is varied while keeping d constant. These results are plotted only for synclastic bending deformation where the applied moments in both in-plane directions are positive. In Figure 5.10 (a), initially the plate is kept fixed at $\omega/\pi = 0.03$, then the moment along x-axis is plotted for increasing ψ. Similarly, in Figure 5.10 (b), z-directional moment is plotted for increasing positive ω/π while keeping the longitudinal curvature $\psi/\pi = 0.02$ fixed. As we see in Figure 5.10 (a), the emergent stiffness gain after scales engagement along x-axis of the plate is highly sensitive on η, and a small variation in η significantly increases the non-linear moment-curvature distribution. For z-directional moment distribution plotted in Figure 5.10 (b), the increasing η has hardly any influential effect on the lateral moment distribution of the plate, which is completely in contrast with the corresponding high η-sensitive characteristic of the longitudinal moment. It is worth mentioning that, in anticlastic loading conditions, the moment-curvature distributions for both the longitudinal and transverse directions exhibit a similar nature as observed in the synclastic case. Although we did not explicitly illustrate it in this discussion to avoid overcrowding the figures, it is important to note the consistency of the moment-curvature responses between the two loading conditions.

Figures 5.11 (a) and (b) demonstrate the effect of dimensionless clearance ratio δ on the moment-curvature distribution of the plate in both the x and z-directions for synclastic deformation shape. The half of the transverse distance between the scales a is varied while keeping d constant to analyze the effect of varying δ. Likewise, in the previous η study, in this δ analysis as well, the plate is initially kept fixed at transverse curvature $\omega/\pi = 0.03$, then the moment along x-axis is plotted for increasing ψ/π (Figure 5.11 (a)). Similarly, in Figure 5.11 (b), moment-curvature distribution along z-axis is plotted for increasing positive ω/π while longitudinal direction initially held fixed at $\psi/\pi = 0.02$. An analysis of gradually increasing δ of the plate from 0.05 to 0.4 shows that the moment-curvature distribution of the plate along both in-plane directions are strongly influenced with the change in δ, and a decreasing nature in the moment-curvature distribution is observed with the increase in δ. It is also noticeable from Figures 5.11 (a) and (b) that δ variation

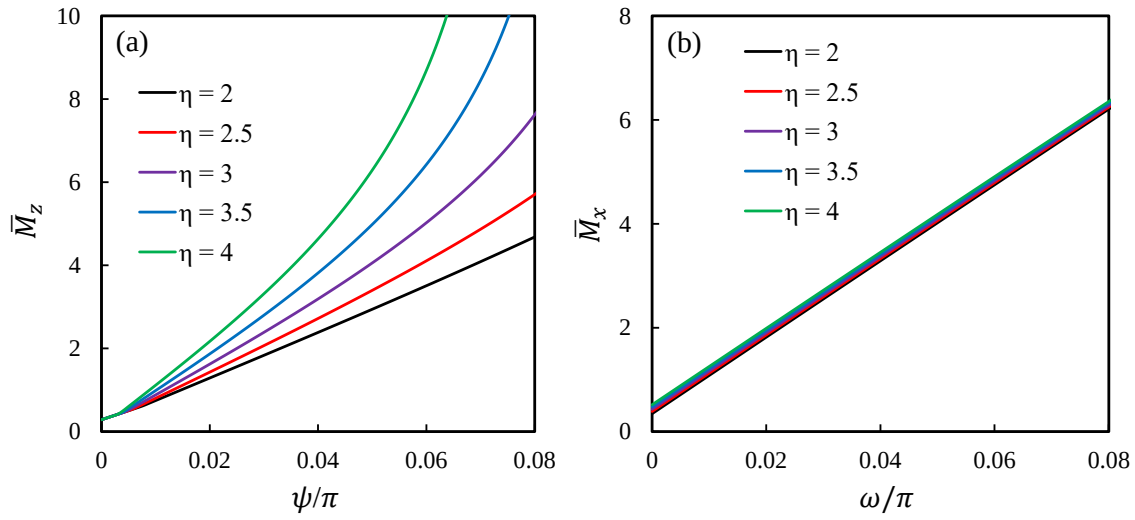

Figure 5.10: $\bar{M}_z$ *vs* ψ/π and $\bar{M}_x$ *vs* ω/π distribution with η for synclastic curvature along: (a) x-axis with ω/π = 0.03 and $\psi/\pi > 0$, (b) z-axis with ψ/π = 0.02 and $\omega/\pi > 0$. Here, $\theta_0 = 5°$, $\beta = 1.4$, and $\delta = 0.1$.

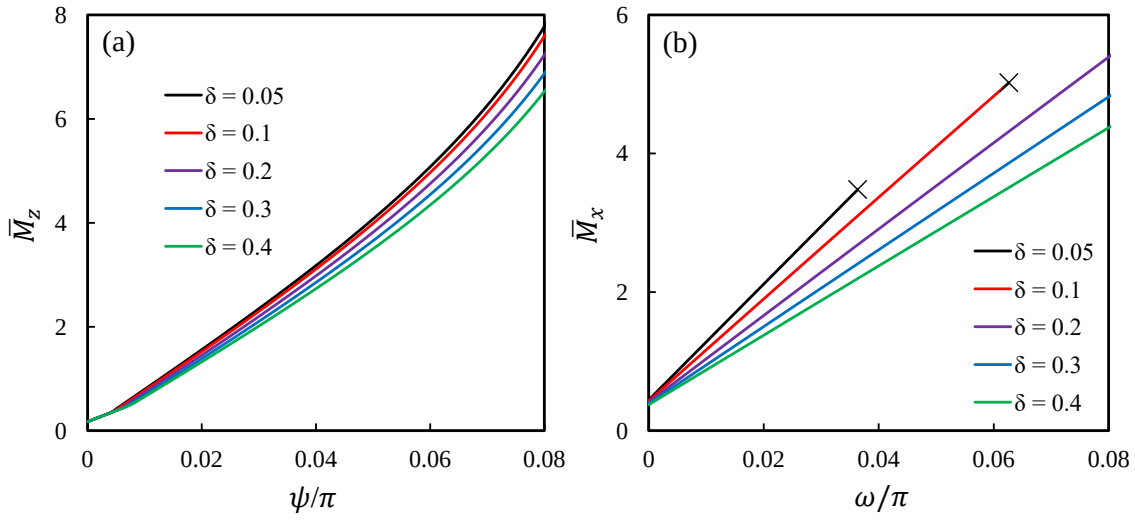

Figure 5.11: $\bar{M}_z$ *vs* ψ/π and $\bar{M}_x$ *vs* ω/π distribution with δ for synclastic curvature along: (a) x-axis with ω/π = 0.03 and $\psi/\pi > 0$, (b) z-axis with ψ/π = 0.02 and $\omega/\pi > 0$. Here, $\theta_0 = 5°$, and $\eta = 3$. ($\times$) in Figure 5.11(b) represents the lateral locking curvature of the plate.

is more significant in transverse directional moment distribution in comparison to the longitudinal direction of the plate. Thus it can be said that with the increase of δ, which corresponds to a decrease in β, the plate structures experience a significant reduction in stiffness, particularly in the z-direction when contrasted with the x-direction of the plate. In anticlastic deformation, the effect of δ on the moment-curvature distribution of the plate is almost the same as the one observed in the synclastic deformation case.

CHAPTER 6: CONCLUSION

In this research, we have developed an analytical model to explore the interaction of two different bending loads along in-plane axes within a biomimetic scale-covered elastic plate system. The model considers scales as rigid rectangular plates, partially embedded at an angle on the elastic substrate's surface. These scales are arranged in a staggered configuration along two in-plane directions. We observed highly complex effects of scale engagement on the system's kinematics and mechanics, notably the nonlinear stiffening effect on the bending-curvature response. These effects were quantified using analytical expressions derived from classical plate theory or Kirchhoff plate theory. Verification was achieved through comparisons with finite-element simulations using commercially available software. The model's result, which is calculated considering the absence of transverse bending loads, align with previous pure 1D bending models.

The kinematic locking analysis of the plate reveals that the presence of transverse bending will decrease the scale engagement as well as the longitudinal locking curvature of the plate. Though the effect of transverse bending in longitudinal locking is not very significant for high η, it becomes noticeable when η is low. It is also clear from the kinematic results that in the absence of longitudinal bending load, with only transverse bending there will be no engagement of scales. Furthermore, a details analysis of locking behavior with various η and δ of the plate showed no significant variation between positive (synclastic) and negative (anti-clastic) transverse bending curvature on the longitudinal locking behavior of the plate. Unlike longitudinal locking, cross-curvature has a very strong effect on the lateral locking of synclastic bending. As longitudinal curvature increases, both lateral locking curvature and lock-free zone in the η *vs* δ plot decrease. From the moment-curvature response of the plate, the anisotropic behavior of the plate is clearly observed. Even the presence of rigid inclusions breaks the diagonal symmetry of the strain energy-contour plot which becomes more evident in the presence of scale engagement. But as scale engages, both

longitudinal and transverse directions bending rigidity has significantly been affected indicating a strong cross-curvature effect for both synclastic and anti-clastic bending modes. It is also observed that likewise 1D case of bending, the overlap ratio has very strong sensitivity on the longitudinal moment distribution of the plate, but this effect is not very prominent in the transverse direction. Dimensionless clearance ratio is also found to play a significant role in the moment-curvature distribution of the plate, especially in z-direction. With the increase of clearance ratio, bending rigidity both in longitudinal and transverse directions is found to be significantly reduced.

This study marks a significant advancement in the understanding and application of biomimetic scale-covered structures, transitioning from simplistic 1D models to more complex and realistic 2D frameworks, which is crucial in real-world practical applications including soft robotics, architectured structural metamaterials, protective armors, and aerospace structures such as mesh reflectors and booms. We, therefore, anticipate that the developed kinematics and mechanics model of 2D plate can further be implemented for analyzing scale-covered 2D plate structures including friction, and fluid structures interactions as well as the nonlinear dynamics problems of the 2D plate.

LIST OF REFERENCES

[1] J. Long, M. Hale, M. Mchenry, M. Westneat, Functions of fish skin: flexural stiffness and steady swimming of longnose gar, lepisosteus osseus, Journal of Experimental Biology 199 (10) (1996) 2139–2151.

[2] J. Huang, X. Wang, Z. L. Wang, Controlled replication of butterfly wings for achieving tunable photonic properties, Nano letters 6 (10) (2006) 2325–2331.

[3] J. Song, S. Reichert, I. Kallai, D. Gazit, M. Wund, M. C. Boyce, C. Ortiz, Quantitative microstructural studies of the armor of the marine threespine stickleback (gasterosteus aculeatus), Journal of structural biology 171 (3) (2010) 318–331.

[4] I. H. Chen, J. H. Kiang, V. Correa, M. I. Lopez, P.-Y. Chen, J. McKittrick, M. A. Meyers, Armadillo armor: mechanical testing and micro-structural evaluation, Journal of the mechanical behavior of biomedical materials 4 (5) (2011) 713–722.

[5] P.-Y. Chen, J. Schirer, A. Simpson, R. Nay, Y.-S. Lin, W. Yang, M. I. Lopez, J. Li, E. A. Olevsky, M. A. Meyers, Predation versus protection: fish teeth and scales evaluated by nanoindentation, Journal of Materials Research 27 (1) (2012) 100–112.

[6] W. Yang, I. H. Chen, B. Gludovatz, E. A. Zimmermann, R. O. Ritchie, M. A. Meyers, Natural flexible dermal armor, Advanced Materials 25 (1) (2013) 31–48.

[7] Z. Sun, T. Liao, W. Li, Y. Dou, K. Liu, L. Jiang, S.-W. Kim, J. H. Kim, S. X. Dou, Fish-scale bio-inspired multifunctional zno nanostructures, NPG Asia Materials 7 (12) (2015) e232–e232.

[8] S. E. Naleway, J. R. Taylor, M. M. Porter, M. A. Meyers, J. McKittrick, Structure and mechanical properties of selected protective systems in marine organisms, Materials Science and Engineering: C 59 (2016) 1143–1167.

[9] B. Wang, W. Yang, V. R. Sherman, M. A. Meyers, Pangolin armor: overlapping, structure, and mechanical properties of the keratinous scales, Acta biomaterialia 41 (2016) 60–74.

[10] W. B. A. Bezerra, S. N. Monteiro, M. S. Oliveira, F. S. da Luz, F. da Costa Garcia Filho, L. C. da Cruz Demosthenes, U. O. Costa, Processing and characterization of arapaima gigas scales and their reinforced epoxy composites, Journal of Materials Research and Technology 9 (3) (2020) 3005–3012.

[11] W. Yang, V. R. Sherman, B. Gludovatz, M. Mackey, E. A. Zimmermann, E. H. Chang, E. Schaible, Z. Qin, M. J. Buehler, R. O. Ritchie, et al., Protective role of arapaima gigas fish scales: structure and mechanical behavior, Acta biomaterialia 10 (8) (2014) 3599–3614.

[12] S. Murcia, E. Lavoie, T. Linley, A. Devaraj, E. A. Ossa, D. Arola, The natural armors of fish: A comparison of the lamination pattern and structure of scales, Journal of the mechanical behavior of biomedical materials 73 (2017) 17–27.

[13] Y. Shelef, B. Bar-On, Surface protection in bio-shields via a functional soft skin layer: Lessons from the turtle shell, Journal of the mechanical behavior of biomedical materials 73 (2017) 68–75.

[14] Z. Liu, D. Jiao, Z. Weng, Z. Zhang, Structure and mechanical behaviors of protective armored pangolin scales and effects of hydration and orientation, Journal of the mechanical behavior of biomedical materials 56 (2016) 165–174.

[15] D. Zhu, F. Barthelat, F. Vernereyb, Intricate multiscale mechanical behaviors of natural fish-scale composites, Handbook of Micromechanics and Nanomechanics ed S. Li and X. Gao (2013).

[16] J. Song, C. Ortiz, M. C. Boyce, Threat-protection mechanics of an armored fish, Journal of the mechanical behavior of biomedical materials 4 (5) (2011) 699–712.

[17] D. Zhu, C. F. Ortega, R. Motamedi, L. Szewciw, F. Vernerey, F. Barthelat, Structure and mechanical performance of a “modern” fish scale, Advanced Engineering Materials 14 (4) (2012) B185–B194.

[18] F. J. Vernerey, F. Barthelat, On the mechanics of fishscale structures, International Journal of Solids and Structures 47 (17) (2010) 2268–2275.

[19] R. Ghosh, H. Ebrahimi, A. Vaziri, Contact kinematics of biomimetic scales, Applied Physics Letters 105 (23) (2014) 233701.

[20] H. Ebrahimi, H. Ali, R. A. Horton, J. Galvez, A. P. Gordon, R. Ghosh, Tailorable twisting of biomimetic scale-covered substrate, EPL (Europhysics Letters) 127 (2) (2019) 24002.

[21] R. Martini, Y. Balit, F. Barthelat, A comparative study of bio-inspired protective scales using 3d printing and mechanical testing, Acta biomaterialia 55 (2017) 360–372.

[22] A. Browning, C. Ortiz, M. C. Boyce, Mechanics of composite elasmoid fish scale assemblies and their bioinspired analogues, Journal of the mechanical behavior of biomedical materials 19 (2013) 75–86.

[23] P. Liu, D. Zhu, J. Wang, T. Q. Bui, Structure, mechanical behavior and puncture resistance of grass carp scales, Journal of Bionic Engineering 14 (2) (2017) 356–368.

[24] S. Ghods, S. Murcia, E. Ossa, D. Arola, Designed for resistance to puncture: the dynamic response of fish scales, Journal of the mechanical behavior of biomedical materials 90 (2019) 451–459.

[25] S. Murcia, M. McConville, G. Li, A. Ossa, D. Arola, Temperature effects on the fracture resistance of scales from cyprinus carpio, Acta biomaterialia 14 (2015) 154–163.

[26] W. Yang, B. Gludovatz, E. A. Zimmermann, H. A. Bale, R. O. Ritchie, M. A. Meyers, Structure and fracture resistance of alligator gar (atractosteus spatula) armored fish scales, Acta biomaterialia 9 (4) (2013) 5876–5889.

[27] R. Ghosh, H. Ebrahimi, A. Vaziri, Frictional effects in biomimetic scales engagement, EPL (Europhysics Letters) 113 (3) (2016) 34003.

[28] H. Ebrahimi, M. Krsmanovic, H. Ali, R. Ghosh, Material-geometry interplay in damping of biomimetic scale beams, Applied Physics Letters 123 (8) (2023).

[29] M. Tatari, H. Ebrahimi, R. Ghosh, A. Vaziri, H. Nayeb-Hashemi, Bending stiffness tunability of biomimetic scale covered surfaces via scales orientations, International Journal of Solids and Structures (2023) 112406.

[30] A. Shafiei, J. W. Pro, F. Barthelat, Bioinspired buckling of scaled skins, Bioinspiration & Biomimetics 16 (4) (2021) 045002.

[31] S. Dharmavaram, H. Ebrahimi, R. Ghosh, Coupled bend–twist mechanics of biomimetic scale substrate, Journal of the Mechanics and Physics of Solids 159 (2022) 104711.

[32] H. Ebrahimi, H. Ali, R. Ghosh, Coulomb friction in twisting of biomimetic scale-covered substrate, Bioinspiration & biomimetics 15 (5) (2020) 056013.

[33] H. Ali, H. Ebrahimi, R. Ghosh, Bending of biomimetic scale covered beams under discrete non-periodic engagement, International Journal of Solids and Structures 166 (2019) 22–31.

[34] H. Ali, H. Ebrahimi, R. Ghosh, Tailorable elasticity of cantilever using spatio-angular functionally graded biomimetic scales, Mechanics of Soft Materials 1 (2019) 10.

[35] R. Ghosh, H. Ebrahimi, A. Vaziri, Non-ideal effects in bending response of soft substrates covered with biomimetic scales, Journal of the mechanical behavior of biomedical materials 72 (2017) 1–5.

[36] A. Shafiei, J. W. Pro, R. Martini, F. Barthelat, The very hard and the very soft: modeling bio-inspired scaled skins using the discrete element method, Journal of the Mechanics and Physics of Solids 146 (2021) 104176.

[37] A. N. Karuriya, F. Barthelat, Plastic deformations and strain hardening in fully dense granular crystals, Journal of the Mechanics and Physics of Solids (2024) 105597.

[38] D. Wu, Z. Zhao, H. Gao, An interface-enhanced discrete element model (i-dem) of bio-inspired flexible protective structures, Computer Methods in Applied Mechanics and Engineering 420 (2024) 116702.

[39] F. J. Vernerey, K. Musiket, F. Barthelat, Mechanics of fish skin: A computational approach for bio-inspired flexible composites, International Journal of Solids and Structures 51 (1) (2014) 274–283.

[40] K. Zolotovsky, S. Varshney, S. Reichert, E. M. Arndt, M. Dao, M. C. Boyce, C. Ortiz, Fish-inspired flexible protective material systems with anisotropic bending stiffness, Communications Materials 2 (1) (2021) 35.

[41] M. Connors, T. Yang, A. Hosny, Z. Deng, F. Yazdandoost, H. Massaadi, D. Eernisse, R. Mirzaeifar, M. N. Dean, J. C. Weaver, et al., Bioinspired design of flexible armor based on chiton scales, Nature communications 10 (1) (2019) 1–13.

[42] A. Bahmani, J. W. Pro, F. Barthelat, Vibration-induced assembly of topologically interlocked materials, Applied Materials Today 29 (2022) 101601.

[43] C. Du, G. Yang, D. Hu, X. Han, Low velocity impact behavior of bioinspired hierarchical armor with filling layer, Mechanics of Advanced Materials and Structures 30 (24) (2023) 4982–4995.

[44] F. J. Vernerey, F. Barthelat, Skin and scales of teleost fish: Simple structure but high performance and multiple functions, Journal of the Mechanics and Physics of Solids 68 (2014) 66–76.

[45] N. Funk, M. Vera, L. J. Szewciw, F. Barthelat, M. P. Stoykovich, F. J. Vernerey, Bioinspired fabrication and characterization of a synthetic fish skin for the protection of soft materials, ACS applied materials & interfaces 7 (10) (2015) 5972–5983.

[46] H. Ebrahimi, Mechanics of low dimensional biomimetic scale metamaterials, Phd thesis, University of Central Florida (2021).